ADVANCES IN ATMOSPHERIC SCIENCES, VOL. 26, NO. 3, 2009, 438–450

Mesoscale Predictability of Mei-yu Heavy Rainfall

LIU Jianyong (刘建勇) and TAN Zhe-Min* (谈哲敏)

Key Lab of Mesoscale Severe Weather/MOE, and School of Atmospheric Sciences, Nanjing University, Nanjing 210093

(Received 10 February 2008; revised 21 August 2008)

ABSTRACT

Recently reported results indicate that small amplitude and small scale initial errors grow rapidly and subsequently contaminate short-term deterministic mesoscale forecasts. This rapid error growth is dependent on not only moist convection but also the flow regime. In this study, the mesoscale predictability and error growth of mei-yu heavy rainfall is investigated by simulating a particular precipitation event along the mei-yu front on 4–6 July 2003 in eastern China.

Due to the multi-scale character of the mei-yu front and scale interactions, the error growth of mei-yu heavy rainfall forecasts is markedly different from that in middle-latitude moist baroclinic systems. The optimal growth of the errors has a relatively wide spectrum, though it gradually migrates with time from small scale to mesoscale. During the whole period of this heavy rainfall event, the error growth has three different stages, which similar to the evolution of 6-hour accumulated precipitation. Multi-step error growth manifests as an increase of the amplitude of errors, the horizontal scale of the errors, or both. The vertical profile of forecast errors in the developing convective system indicates two peaks, which correspond with convective instability and the moist physics. The error growth for the mei-yu heavy rainfall is concentrated inside the mei-yu front, and related to moist convective instability and scale interaction.

Key words: mesoscale predictability, error growth, scale interaction, mei-yu front precipitation

Citation: Liu, J. Y., and Z.-M. Tan, 2009: Mesoscale predictability of mei-yu heavy rainfall. *Adv. Atmos. Sci.*, **26**(3), 438–450, doi: 10.1007/s00376-009-0438-9.

1. Introduction

It is widely appreciated that forecasts of atmospheric motion have a predictability limit because of initial condition uncertainty and the chaotic nature of the atmosphere. In meteorology, the word "predictability" was given a very special meaning by Thompson (1957). He found that numerical weather prediction was sensitive to errors in initial conditions, and that the forecast error growth is related to the horizontal scale of initial errors. With improvements in instrumental precision and network density, observational data is more accurate, but small amplitude, small scale errors are inevitable. Therefore, errors can not be completely removed from the initial conditions due to data analysis and the uncertainty of observations. Even if the forecast models and initial conditions are more accurate than presently available, the errors due to small scale motions may grow rapidly so that they place an effective limit on the predictive skill (Lorenz, 1969).

Predictability research has initially focused on mid-latitude synoptic weather systems and medium-range (3–5 days) forecasting. In this setting, the error growth is primarily determined by the evolution of baroclinic perturbations (Molteni and Palmer, 1993). The first studies of mesoscale predictability using an actual regional weather forecast model were conducted by Anthes et al. (1985). They indicated that mesoscale motions enjoyed enhanced predictability, presumably because mesoscale phenomena are strongly constrained by topography and other local features. But Errico and Baumhefner (1987) demonstrated that strong dissipation and the lack of boundary perturbations dominated the results of Anthes et al. (1985). For mesoscale weather systems associated with moist convection, the rapid growth of forecast errors is generally dependent on convective instability and latent heat release (Tan et al., 2004, hereafter Tan04), so that the growth and structure of

*Corresponding author: TAN Zhe-Min, zmtan@nju.edu.cn

forecast errors is more complicated than that in the dry atmosphere. Using the fifth-generation Pennsylvania State University (PSU)-National Center for Atmospheric Research (NCAR) Mesoscale Model (MM5, Dudhia, 1993), Zhang et al. (2002, hereafter ZSR02) and Zhang et al. (2003, hereafter ZSR03) investigated the forecast errors and mesoscale predictability for the 24–25 January 2000 "surprise" snowstorm along the east coast of the United States. They found that small initial errors in the forecast model grew rapidly at small scales, quickly saturated, and subsequently spread upscale. The single convective system was first influenced by the initial errors, and then error amplitude in this region increased and saturated. After forecast errors spread upscale, they subsequently contaminated cyclone system forecasting. In a general framework, the mesoscale predictability and error growth characteristics have been identified in idealized moist baroclinic waves by Tan et al. (2004).

The current skill associated with warm season rainfall predictions is relatively low, both by absolute standards and relative to predictions of winter season weather systems with strong baroclinicity (Olson et al., 1995; Fritsch et al., 1998). For warm season rainfall forecasting, small scale and small amplitude initial errors rapidly grow, saturate and subsequently upscale, ultimately limiting forecast skill (Bei and Zhang, 2007; Zhang et al., 2006). Using truncated perturbations at different scales, Tribbia and Baumhefner (2004) investigated the error energy spectrum cascade. They found both small scale and large scale errors could contaminate forecasting, and the scale interaction of forecast errors ultimately limited prediction. Carbone et al. (2002) identified precipitation episodes in warm season precipitation systems, which were defined as time-space clusters of heavy precipitation with long lifecycles that often resulted from organized mesoscale or large-scale weather systems such as squall lines or mesoscale convective complexes. These characteristics of coherent rainfall patterns enhanced the predictability of warm season rainfall. Tuttle and Carbone (2004) subsequently indicated that the episodes were caused by the cold air pool, low-level shear, and moisture convergence. Therefore, scale interaction has an important role in the limitation of the predictability of warm season rainfall.

The primary objective of this paper is to study the mechanism of rapid error growth associated with warm season precipitation episodes along the mei-yu front over the Yangtze River-Huaihe River valleys in East China. In general, the mei-yu front is a moist, quasi-stationary front with weak baroclinicity, which contains weather systems ranging from the mesoscale to synoptic scale (Akiyama, 1990). The organized mesoscale and subsynoptic scale systems related to the mei-yu front include the low-level jet (LLJ), upper-level jet (ULJ), mesoscale convective systems (MCS), mesoscale convective vortices (MCV), low-level shear lines, etc. The mei-yu front is also affected by the subtropical high over the Western Pacific and the cold trough over northern China (Tao, 1980). A high moisture zone is sustained near the quasi-stationary mei-yu front, which determinates the direction of the low-level vortices and MCSs propagating from the southwest to the Yangtze River-Huaihe River valleys in East China. The propagation of the Southwest Vortex, which is a low-level vortex associated with the terrain, helps maintain the longevity of episodes. For the mei-yu front, Bei and Zhang (2007) investigated impacts of initial errors' scale and amplitude on the mesoscale predictability of heavy precipitation systems. They found the larger-scale, larger-amplitude initial uncertainties generally led to larger forecast divergence, though small-scale and small-amplitude error growth rapidly limited predictability at the mesoscale. They mainly focused on the predictability of local rainfall near Wuhan; however, longer lived rainfall episodes within the mei-yu front were not considered.

The paper is structured as follows. A brief synoptic overview is presented in section 2. The model and experimental design are described in section 3. Section 4 analyzes the time-space distribution and evolution of forecast errors within episodes of rainfall along the mei-yu front. The multi-step error growth is discussed in section 5. In section 6, the vertical profile of forecast errors is explored. A summary and discussions are presented in section 7.

2. Synoptic overview

Between 0000 UTC 4 July and 0000 UTC 6 July 2003, heavy rainfall spread all over the Yangtze River-Haihe River valleys in East China. The maximum precipitation at a single station was 356.9 mm during 24 h, which was twice the previous record. This heavy rainfall event belonged to the third rainfall stage during the 2003 mei-yu season over the Yangtze River-Huaihe River valleys in East China. Figure 1 shows the 850 hPa horizontal wind field, the equivalent potential temperature at 700 hPa in the upper panel, and the 500 hPa geopotential height and 400 hPa horizontal wind field in the lower panel at 0000 UTC 4 and 0000 UTC 5 July. These data are from NCEP final analysis data. The quasi-stationary convergence zone spanning from southwestern China to the Yangtze River-Huaihe River valleys is known as the mei-yu front. Though the temperature gradient was so small, a high horizontal gradient of equivalent potential temperature was ma-

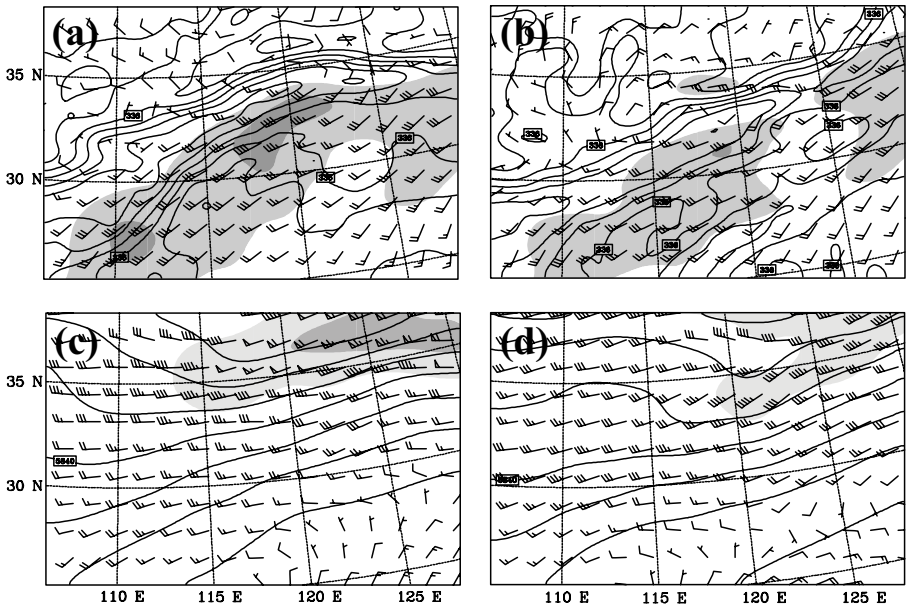

Fig. 1. Upper panels: NCEP global analysis equivalent potential temperature at 700 hPa (solid contours, 4 K intervals), horizontal 850 hPa wind (full barb=4 m s^{-1}) and low level jet at 850 hPa (shaded$\geqslant$12 m s^{-1}, 6 m s^{-1} intervals) at (a) 0000 UTC 4 July and (b) 0000 UTC 5 July 2003. Lower panels: 500 hPa geopotential height (solid contours, 20 dagpm intervals), horizontal 400 hPa wind (full barb=4 m s^{-1}) and upper level jet at 400 hPa (shaded$\geqslant$20 m s^{-1}, 10 m s^{-1} intervals) at (c) 0000 UTC 4 July and (d) 0000 UTC 5 July 2003.

intained near the mei-yu front due to the convergence of moisture.

Before the onset of this heavy rainfall, there was a strong LLJ with horizontal wind speeds greater than 12 m s^{-1} at 850 hPa. The isotach of 12 m s^{-1} extended 400 km from west to east at 0000 UTC 4 July, and contained two mesoscale LLJs (hereafter mLLJ) (Fig. 1a). The western mLLJ was immediately adjacent to this event, and located south of the mei-yu front in Hunan Province, transmitting water vapor from South China to the Yangtze River-Huaihe River valleys. On one hand, the LLJ supplied the vertical component of vorticity resulting from low-level shear, and organized the episodes of rainfall. On the other hand, the LLJ coupled with the ULJ, which sustained the convection of the mei-yu front as seen in a modeling study (Liao and Tan, 2005). Comparison of Fig. 1b with Fig. 1a shows that the LLJ intensified again until 0000 UTC 5 July. Also, a new MCS developed at simulated +21 h (Liao and Tan, 2005). Moreover, the ULJ moved southward, further coupling with the LLJ (Fig. 1d).

A series of MCSs developed one after the other along the quasi-stationary convergence zone, and propagated from west to east on 4–5 July. Based on the satellite brightness temperature from GEOS-9 channel one, three MCS (defined as MCS1, MCS2, and MCS3) led to the heavy precipitation event (Fig. 2). At 1200 UTC 4 July, MCS1 originated near Wuhan (30.61°N, 114.13°E) and propagated downstream. When MCS1 rounded Dabie Mountain, it split into two parts. After 6 hours, the two separate parts of MCS1 merged together and decayed. In the meantime, the cold pool induced by the MCS1 rainfall triggered a new mesoscale convective system (MCS2), which brought over 140 mm in rainfall. Accompanying the 500 hPa short-wave trough moving south (Figs. 1c and 1d), MCS1 was renewed and became more organized (MCS3). The corresponding MCV made several separate convective centers which merged and developed, which induced a second rainfall period in Jiangsu Province. This episode had coherent rainfall similar to that seen in Carbone et al. (2002) and Wang et al. (2004). The details of the evolution of MCSs and MCVs during this heavy rainfall event, and the scale interaction in the mei-yu front can be found in Liao and Tan (2005) and Chu et al. (2007).

3. Numerical models and experimental design

3.1 *Numerical models and initial condition*

The non-hydrostatic mesoscale model MM5 version 3.6 (Dudhia, 1993) was used for this study. The numerical simulation employs two horizontal domains

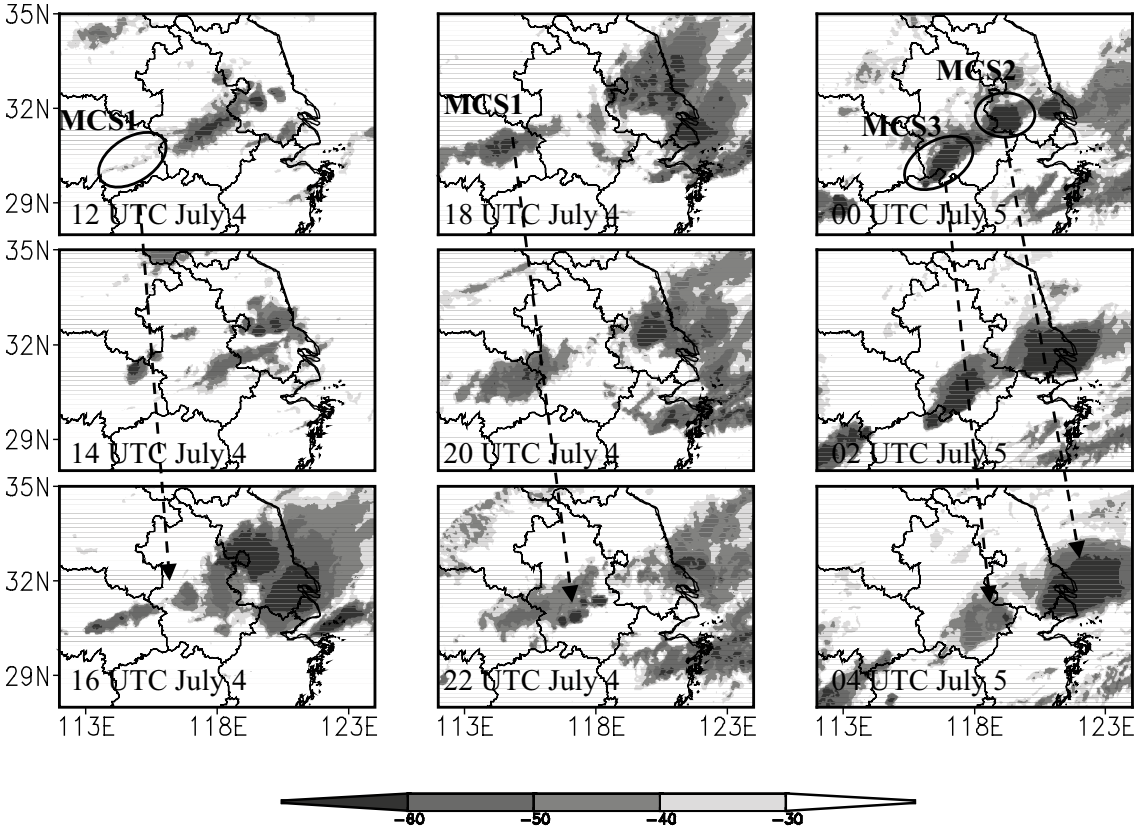

Fig. 2. Satellite brightness temperature (TBB) valid between 1200 UTC 4 July and 0400 UTC 5 July 2003, at two hour intervals.

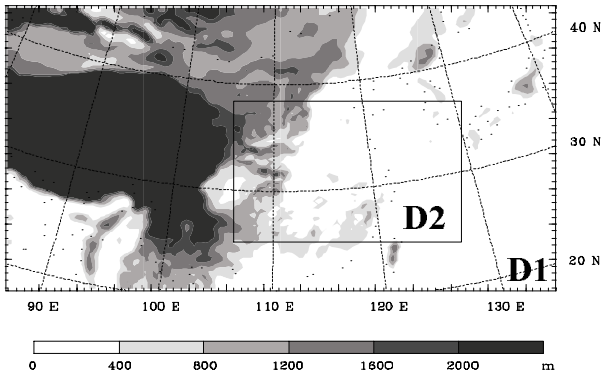

Fig. 3. MM5 model domains and terrain. The grid resolutions of domain 1 (D1) and domain 2 (D2) are 36 and 12 km, respectively.

(D1 and D2) with 36- and 12-km grid resolution, respectively. Considering the effect of the terrain and water vapor sources on the mei-yu front, the 36 km coarse domain employs 142×182 horizontal grid points, which covers the greater part of the Tibetan Plateau and contains part of the Bay of Bengal and the East China Sea. The inner domain (D2) has 184×121 horizontal grid points, and both domains have a total of 23 vertical layers, which covers the main body of the mei-yu front in East China. The topography within D1 is presented in Fig. 3. To maintain the same lateral boundary during different numerical simulations of inner domain (D2), one-way nesting is employed in this study. The Betts-Miller cumulus parameterization (Betts and Miller, 1986), the Blackadar planetary boundary layer scheme (Blackadar, 1979), the microphysics scheme with simple ice phase, and simple radiation parameterization are used in both domains. Final analysis data (1° horizontal resolution, 26 vertical levels and a 6-hourly updating frequency) from Final Global Data Assimilation System (FNL) and conventional observational data were used for the model's initial and boundary conditions.

3.2 *Experiment design*

To investigate the characteristics and the mechanism of error growth associated with a mei-yu heavy rainfall event in warm season, control and perturbation experiments were designed. In the control experiment, the evolution and structure of the mei-yu front and the rainfall episodes are reproduced. The outer domain D1 is initialized at 0000 UTC 4 July, and integrated for 48 hours in order to supply initial conditions and lateral conditions for D2. In view of the initial-stage

adjustment, D2 is initialized by forecast results from D1 at 0300 UTC 4 July (hereafter referred to as CNTL-D2). In CNTL-D2, the evolution of MCSs, the development of MCVs within the mei-yu front, and the total precipitation were simulated consistent with the observations (not shown). The details of the simulation of MCSs and precipitation during this heavy rainfall event can be found in Liao and Tan (2005). The perturbed experiment (hereafter referred to as CNTL-D2P) used CNTL-D2 in D2 and examined the sensitivity of the forecast to initial errors. Additional initial errors were added in CNTL-D2P, and integrated for 48 hours with the same boundary conditions as in CNTL-D2. The perturbations added to the initial conditions consist of random errors after those in Tan04, with Gaussian noise added to the temperature field in D2. The noise has a zero mean, standard deviation $T' = 0.2$ K, and is independent at each grid point and each grid level. Since our interest lies in the error growth from initial small amplitude and small scale Gaussian noise, the numerical model was taken as perfect, and was able to simulate the gross features of this heavy rainfall event as shown in Liao and Tan (2005). To reduce sources of errors in the numerical model, the lateral, upper, and lower boundary conditions do not employ noise.

4. Error growth in mei-yu heavy rainfall

We begin by examining the evolution of small scale, small amplitude initial errors in CNTL-D2 and CNTL-D2P. Figure 4 shows the 500-hPa meridional wind difference at 6, 12, 24, and 36 h, where the thick lines from southwest to northeast represent 338 K equivalent potential temperature. The isolines of the 338 K equivalent potential temperature surround the mei-yu front where moist-convective motion prevails; therefore, this can be regarded as the boundary of mei-yu front. The initial random errors added to the temperature field have decayed everywhere except for a narrow zone near the mei-yu front and the southeast quadrant of the short wave at first 3 h.

By 6 h, the horizontal wind difference has grown to a maximum of 1.6 m s^{-1}, but the horizontal scale

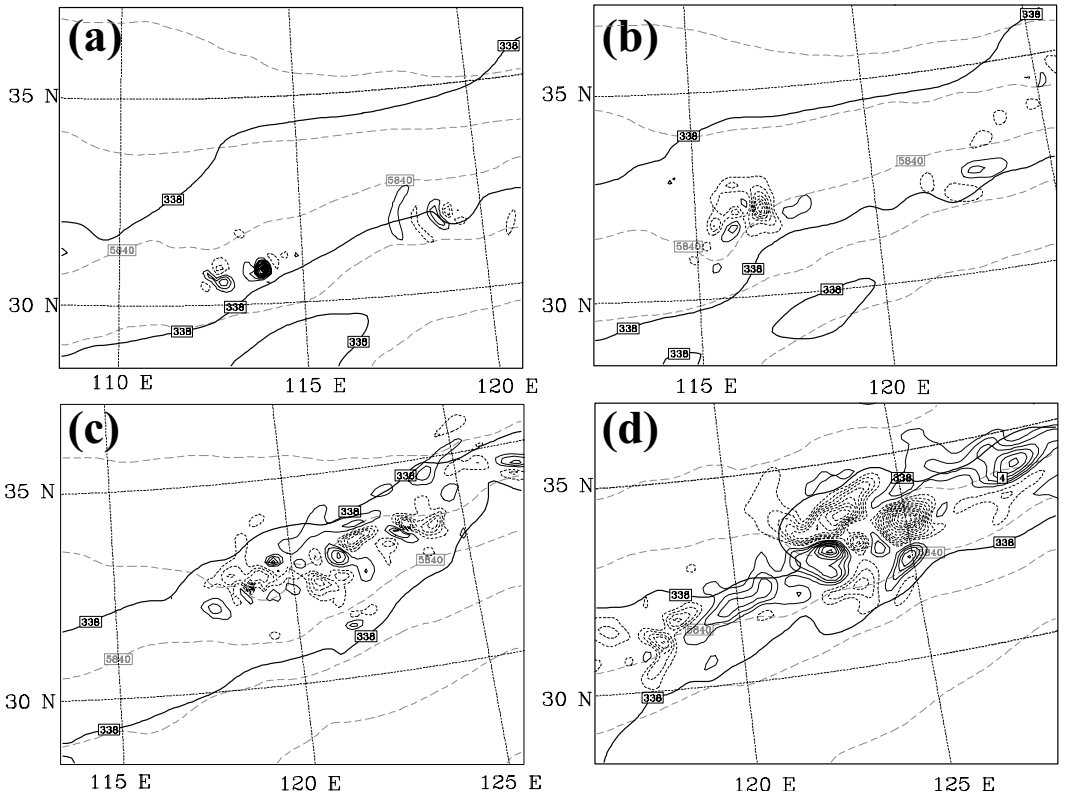

Fig. 4. The 500 hPa meridional wind difference (thin lines for positive; short dashed lines for negative) between CNTL-D2 and CNTL-D2P valid at (a) 6 h, (b) 12 h, (c) 24 h, and (d) 36 h of the nested domain simulation in D2. Contour intervals are 0.2 m s^{-1} for (a), 0.5 m s^{-1} for (b), and 1 m s^{-1} for (c) and (d), respectively. The 500 hPa geopotential height (long dashed lines, 20 dagpm intervals) and 338 K isolines of the equivalent potential temperature at 500 hPa (thick lines) denote the boundary of the mei-yu front. The display window boundaries move east with time.

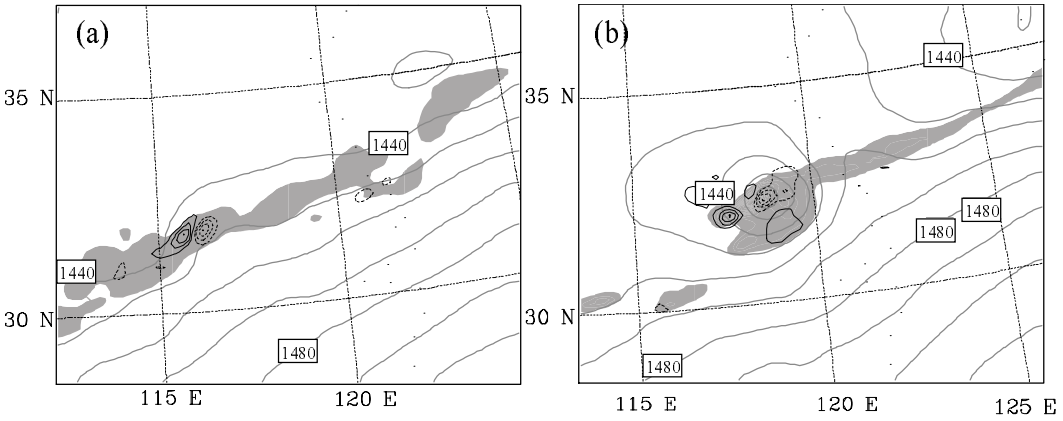

Fig. 5. The 6-h accumulated precipitation difference (thin lines for positive; short dashed lines for negative; contour interval 5 mm) between CNTL-D2 and CNTL-D2P valid at (a) 12 h and (b) 24 h. The 850 hPa geopotential height (10 dagpm intervals) in CNTL-D2 is overlaid (thick lines). Areas with 6-h accumulated precipitation greater than 10 mm are shaded. The display windows are the same as in Fig. 4.

is only about 50 km because it grows in the form of a single convective system (Fig. 4a). In the following 6 h, the wind differences continue to grow, and reach 2.9 m s^{-1} (Fig. 4b), which corresponds to the value in Tan04, although the horizontal wind difference is only about 0.2 m s^{-1} at 3 h which is smaller than the value of 0.5 m s^{-1} in Tan04. The errors growth is faster in this event after the convective systems occurred compared to the moist baroclinic wave in Tan04. At this time, the spatial scale and extent of errors increase greatly, reaching roughly 200 km at 12 h. Subsequently, the short-wave trough at 500 hPa moves even faster than the propagation of errors, and then the meridional wind differences don't only concentrate on the southeast side. This indicates that baroclinic instability is not the main mechanism of the growth and propagation of differences in this case; moreover, wind differences remain inside the mei-yu front, which means the mei-yu front could limit error growth in the horizontal scale (Fig. 4c). At 36 h, the wind differences cover the whole mei-yu front and the differences begin to organize (Fig. 4d).

Figure 5 shows the 6-h accumulated precipitation difference between CNTL-D2 and CNTL-D2P valid at 12 and 24 h. The maximum differences are all roughly about 25 mm at 12 h and 24 h, and their horizontal location corresponds broadly to that of the maximum wind difference at those same times (Figs. 4b and 4c). Because convective precipitation and nonconvective precipitation both contribute toward the total precipitation, total precipitation is best suited to represent the activity of moist convection in mei-yu front. The 6-h accumulated precipitation differences locate in the active zone of moist convection, as indicated by the shaded area of 6-h accumulated precipitation (greater than 10 mm) in CNTL-D2 (Fig. 5). From Fig. 4 and Fig. 5, we find that the initial error growth mainly related to the moist convection. In the first 3 h, inactivity of moist convection is responsible the forecast difference of 500 hPa meridional wind, which is smaller than that in Tan04, though both initial errors had the same scale and amplitude.

To further compare the error growth in this mei-yu heavy rainfall event within a moist baroclinic wave, as in ZSR03 and Tan04, the difference total energy (DTE) is defined as

$$\mathrm{DTE} = \frac{1}{2}(U'^2_{i,j,k} + V'^2_{i,j,k} + \kappa T'^2_{i,j,k}) \qquad (1)$$

where U', V' are the difference wind components, T' is the difference temperature between CNTL-D2 and

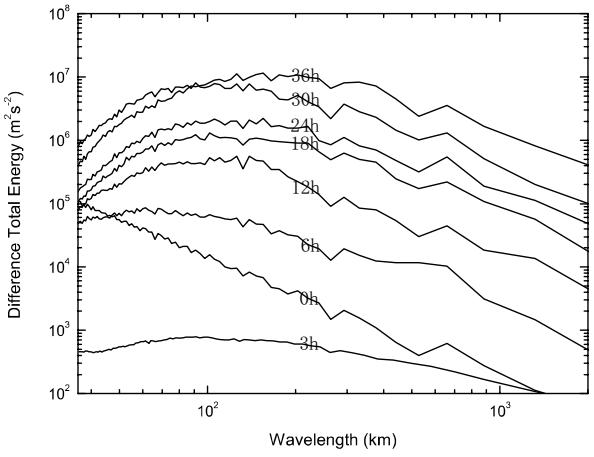

Fig. 6. Power spectra of DTE (m^2 s^{-2}) plotted every 6 h from 0 h, as well as at 3 h.

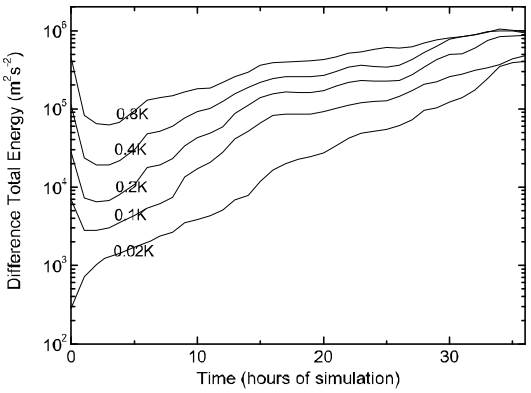

Fig. 7. The evolution of DTE ($m^2\ s^{-2}$) estimated for differences between CNTL-D2 and CNTL-D2P with time, but for standard deviations of 0.02, 0.1, 0.2, 0.4, and 0.8 K in the initial errors.

CNTL-D2P, $\kappa = c_p/T_r$ (with reference temperature T_r=287 K and c_p the specific heat at constant pressure), and i, j, and k run over D2 horizontal points and vertical layers.

As shown in Tan04, the evolution of power spectrum of DTE with time provides the behavior of error growth in different scales. Figure 6 shows the power spectrum analysis of DTE. The spectral density of the initial random perturbation is inversely proportional to the horizontal scale. Over the first 3 h, the smaller-scale (<100 km) components of DTE spectrum decreased rapidly because of the initial adjustment of the numerical model, which is also related to the initial condition without moist convective process. Snyder et al. (2003) and Tan04 explain the similar behavior with numerical diffusion. Compared to the moist baroclinic waves in Tan04, the spectral width of the decaying errors is wider within the range from 20 km to 800 km, but smaller scale errors show relatively weak decreases. Because the baroclinic instability in the mei-yu front system is too weak, large-scale errors can not be rapidly organized or amplified. In the meantime, moist convection in the mei-yu front is more active, so that convective instability becomes stronger and then the convective-scale errors more slowly decrease though numerical diffusion. Over the entire forecast period to 36 h, the DTE grows steadily at larger wavelengths. DTE also increases rapidly at smaller wavelengths over the first 12 h, but the smaller scale errors subsequently reach saturation, and the growth speed of the smaller scale DTE becomes slow. The peak of the spectrum gradually migrates from smaller to larger scales with time, and the spectral peak covers 80–120 km by 36 h, which is less than what was seen by ZSR03 (700–1000 km after 36 h). The slow inverse cascade of errors from small to large scales has been verified with a two-dimensional closure model by Lorenz (1969).

The spectral density characteristics of DTE in this event are closed related to the strongly convective instability and weak baroclinicity in the mei-yu front. In this event, a series of MCSs are developing along the mei-yu front, whose horizontal scales are about 100 km. The propagation of the low-level vortex induces new MCSs one after another, accompanied by low-level shear lines, the short-wave trough, and the moisture gradient zone. The small-scale errors produced by the older convective systems contaminate the distribution of the low-level shear and the moisture gradient so as to influence the development of new convective systems. In this event, there is coherent error growth, with horizontal scales ranging from the subsynoptic scale to smaller scales. The optimal growth of the errors has a relatively wide spectrum ranging from 80 km to 120 km, and convective-scale error growth prevails.

To illustrate the influence of initial errors' amplitude on the error growth, we have performed another experiment configured exactly the same as CNTL-D2P, except using 0.02, 0.2, 0.4, and 0.8 K for the standard deviation of the white noise. Figure 7 shows the evolution of the DTE with time for the different amplitudes of initial errors. When the initial errors are only 0.02 K, the errors grow steadily over the entire forecast, and the decreasing stage of CNTL-D2P is absent. For the initial small amplitude errors, the effect of diffusion is relative weak and smaller than the nonlinear to error growth in the initial stage. Though the DTE ratio of the cases of 0.02 and 0.8 K initial errors is about 10^3, the DTEs with the different initial error levels all have the same order by 36 h (Fig. 7). Moreover, the overall character of the evolution of the power spectrum with time is not sensitive to the amplitude of the small scale initial errors (not shown). This further demonstrates that the mechanisms of the error growth mainly depend on the intrinsic atmospheric instability. However, the smaller the initial errors are, the faster they grow; this behavior indicates that the error growth is nonlinear. This dependence of the error growth rate on the initial amplitude is consistent with the physical arguments by Lorenz (1969). Even if observational instrument precision has large advances over time, the forecast errors will still depend on not only initial uncertainty but also the convective instability.

5. The error growth in different stages of the rainfall

As shown in Fig. 5, the error growth is concentrated in the mei-yu front from southwest to northeast, which is different from the result of Tan04, where growth concentrated on the southeast side of the up-

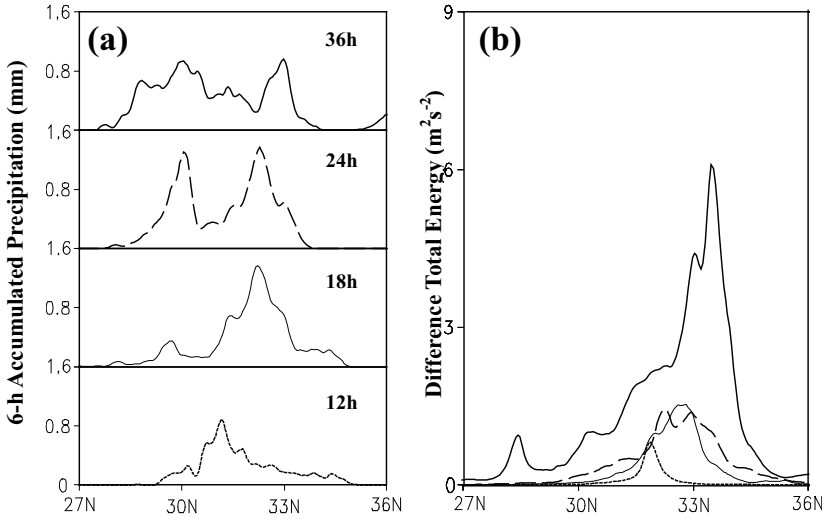

Fig. 8. (a) The zonal mean of 6-h accumulated precipitation (SAP), and (b) the zonal mean of DTE (MDTE), both at 12 h (dotted line), 18 h (thin line), 24 h (dashed line), and 36 h (thick line).

per trough in the moist baroclinic wave case. There are several separate MCSs in a line along the mei-yu front (Fig. 2), and the distribution of errors is irregular along this direction. The cross-frontal distribution of error is relatively regular and has a distinctive structure. Over the entire 36 h forecast, the direction of the mei-yu front approximately parallels the equator, and this then favors the calculation of cross-frontal errors. To investigate the relationship between error growth and moist convection, the cross-frontal zonal mean DTE (hereafter MDTE) is analyzed here, which is used to describe the horizontal characteristics of errors across the mei-yu front. Figure 8 shows the MDTE and the zonal mean of 6-h accumulated precipitation across the mei-yu front at different stages. As shown in Fig. 8, the horizontal distribution of MDTE with latitude corresponds with that of the zonal mean 6-h accumulated precipitation (hereafter SAP), and their evolution is similar, as well. Over the initial stage (∼12 h), there is only one maximum of SAP and one peak for MDTE. After 24 h of simulation time, the MDTE has several peaks accompanied by a few maxima of SAP (Fig. 8b). Comparison of Figs. 8b with Fig. 8a further verifies that error growth mainly depends on mesoscale moist convection.

Considering the adjustments of the numerical simulation and the MCS development, after 10 h simulation time, the MDTE could be curve-fit every hour with a normal distribution. Based on the growth of the amplitude and the cross-frontal horizontal scale of errors during 12–36 h, the MDTE as shown in Fig. 8b could be fit with the following formulation:

$$\mathrm{MDTE}(t,y) = D_0(t)e^{-2\left(\frac{y-y_c}{L_e(t)}\right)^2}\ , \tag{2}$$

where $D_0(t)$ is the amplitude of MDTE at time t, y_c is the meridional location of the maximum of MDTE, y is the meridional coordinate, and $L_e(t)$ is the cross-frontal horizontal scale of errors. By fitting the data from Fig. 8b, $D_0(t)$ and $L_e(t)$ are functions of time, and have different forms at different stages of error growth. They are given as follows:

$$D_0(t) = \begin{cases} -547.0 + 224.0e^{t/4.5} & 10 \leqslant t \leqslant 15\ , \\ 2023.8 + 25551.7e^{-t/8.0} & 15 < t \leqslant 21\ , \\ 3790.9 + 0.386e^{t/3.4} & 21 < t \leqslant 36\ , \end{cases} \tag{3}$$

and

$$L_e(t) = \begin{cases} 24.0 + 2.7t & 10 \leqslant t \leqslant 15\ , \\ 263.0 - 5284.2e^{-t/4.5} & 15 < t \leqslant 21\ , \\ 240.0 & 21 < t \leqslant 36\ , \end{cases} \tag{4}$$

where t is the hour.

Figure 9 shows the evolution of $D_0(t)$ and $L_e(t)$ with time. As shown in Fig. 9, there are three different stages for the evolution of $D_0(t)$, which are consistent with the variation of the 1 h maximum grid precipitation produced by the different MCSs with time (Fig. 10). When the rainfall of MCS1 grows quickly at 10–15 h, $D_0(t)$ also increases exponentially with time (Fig. 9). At 15 h of simulation time, a new MCS (MCS2) has just developed and MCS1 begins to weaken. From 15 to 21 h of simulation time, the total convective intensity becomes weaker, though the total area of precipitation produced by MCS1 and MCS2 grows (Fig. 10). Therefore, the amplitude $D_0(t)$ decreases exponentia-

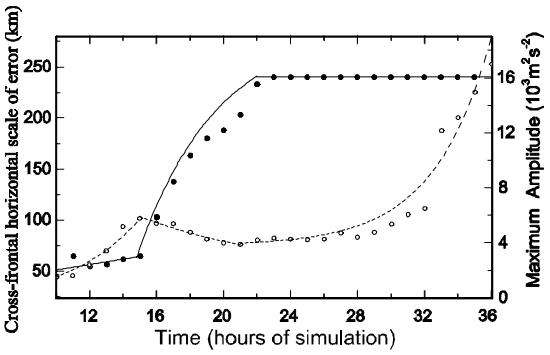

Fig. 9. The evolution of the amplitude $D_0(t)$ (10^3 m^2 s^{-2}, dashed line) and cross-frontal horizontal scale $L_e(t)$ (km, solid line) of MDTE with time. The fitted lines follow Eqs. (3) and (4), from 10 h to 36 h.

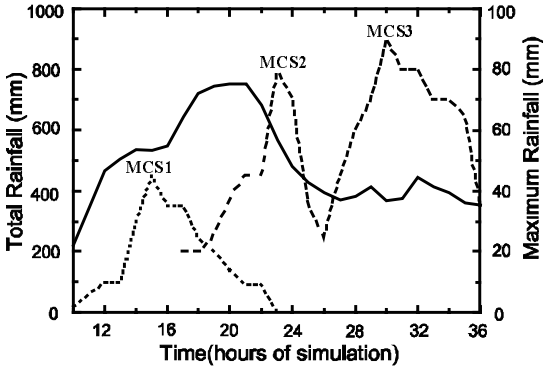

Fig. 10. The 1-h accumulated area precipitation (solid line; mm) in D2 and the 1-h maximum grid rainfall (mm) for different MCSs from 11 h to 36 h. The dotted lines are for MCS1, the dashed lines are for MCS2 and MCS3.

lly in this period, but the rate of decay is smaller than the rate of growth in the first stage. Accompanied by the development of a new MCS (MCS3), $D_0(t)$ secondly grows exponentially due to the convective instability related to MCS3.

Similar to the evolution of $D_0(t)$, the cross-frontal horizontal scale of the error $L_e(t)$ could be also decomposed into three different stages, but has a different trend of variability (Fig. 9). In the first stage (10–15 h), $L_e(t)$ increases linearly due to the single MCS1 intensifying (Fig. 10). With the development of MCS2 and weakening of MCS1 (16–21 h), $L_e(t)$ grows exponentially with time, which was mainly related to the impact of convective heating of MCS1 and convective instability of MCS2, though $D_0(t)$ decays in the meantime. After 21 h of simulation time, $L_e(t)$ maintains a size of about 240 km, corresponding to the cross-frontal scale, which is the third stage for the evolution of $L_e(t)$.

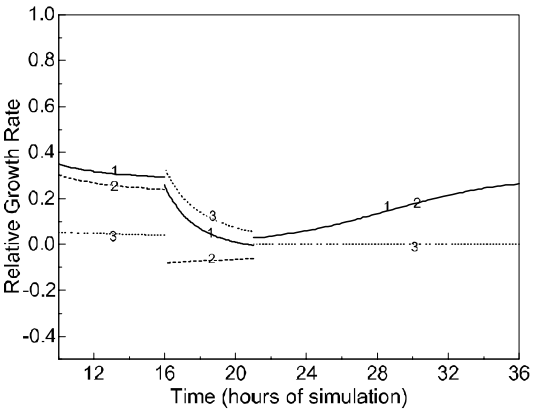

Fig. 11. The relative growth rate of MDTEav (solid line, 1), the amplitude of errors $D_0(t)$ (dashed line, 2), and the cross-frontal horizontal scale of errors $L_e(t)$ (dotted line, 3) during three stages of error growth from 10 h to 36 h. After 21 h, the relative growth rate of MDTE$_{\rm av}$ and that of the amplitude $D_0(t)$ overlap.

The evolution of amplitude and cross-frontal scale of errors with time indicate the error growth in this heavy rainfall event depends on not only the local convective instability, but also scale interaction in the mei-yu front. In the second stage (15–21 h), $D_0(t)$ decreases with a relatively smaller rate; however, the cross-frontal horizontal scale of errors grows exponentially with time, which results in the peak of the error spectrum migrating from small scale to mesoscale (Fig. 6).

Integration of Eq. (2) with y from $y_c - L_e/2$ to $y_c + L_e/2$, obtains a relative growth rate for the average MDTE (hereafter MDTE$_{\rm av}$),

$$\frac{d\ln \mathrm{MDTE}_{\rm av}}{dt} = \frac{d\ln D_0}{dt} + \frac{d\ln L_e}{dt}\,. \qquad (5)$$

Figure 11 shows the evolution of the relative growth rate of MDTE$_{\rm av}$, $D_0(t)$ and $L_e(t)$ with time. It is evident that $D_0(t)$ and $L_e(t)$ have different contributions to the relative growth rate of MDTE$_{\rm av}$. When there is only one single MCS rapidly developing (Stages 1 and 3), the relative growth rate of mainly depends on $D_0(t)$. In this stage, the errors grow mainly with increasing amplitude, which relates to the convective instability. However, in the second stage, $L_e(t)$ mainly determined the relative growth rate of MDTE$_{\rm av}$, where multiple MCSs were developed within the life cycle. Moreover, as shown in Eq. (5) the growth of $L_e(t)$ would reduce $D_0(t)$ if remains constant. When $L_e(t)$ reaches the cross-frontal scale, the error growth rate is mostly dependent on $D_0(t)$.

Along the mei-yu front, the errors propagate downstream with the rainfall moving eastward. Though

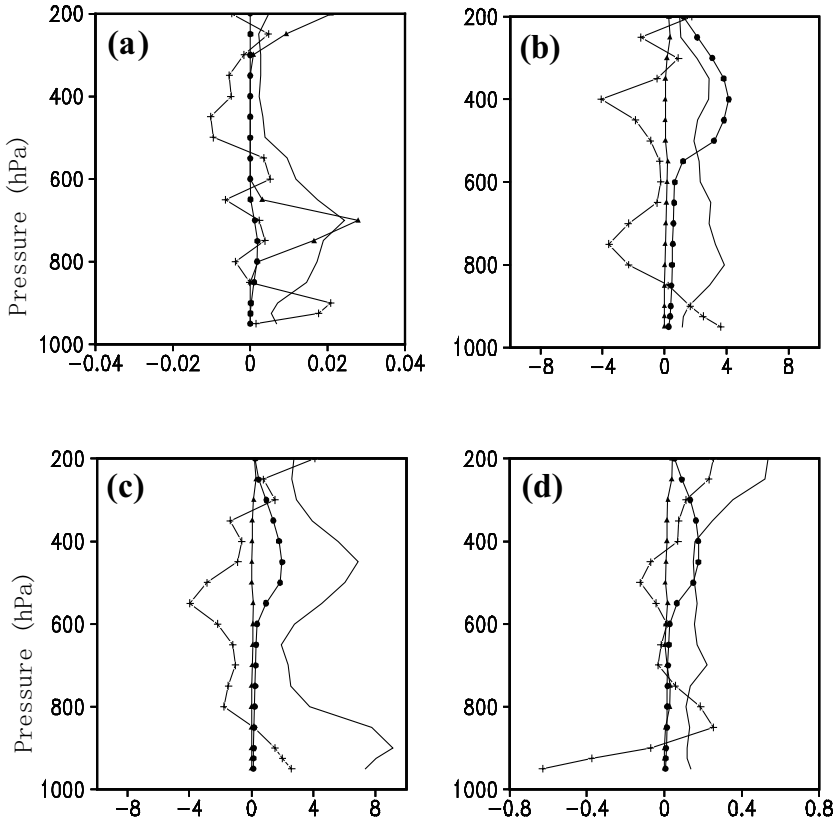

Fig. 12. The vertical profile of the horizontal mean of DTE (HDTE) (no mark; $m^2\ s^{-2}$), the horizontal divergence (cross marker; $2 \times 10^{-3}\ s^{-1}$, $2{\times}10^{-5}\ s^{-1}$, $2{\times}10^{-5}\ s^{-1}$ and $2 \times 10^{-4}\ s^{-1}$ for (a), (b), (c) and (d), respectively), the rain water (circle marker; 0.5 g kg^{-1}) and the cloud water (triangle marker; 0.5 g kg^{-1}) at the different stage. (a) non convection area, (b) the developing convective system, (c) the mature convective system, (d) the old convective system deceasing and new one initial development.

the peaks of errors and precipitation are overlapping, the small-amplitude errors propagate even faster than precipitation systems, due to the moist convection induced by the wave-like mechanism in the coherent rainfall pattern (Carbone et al., 2002; Wang et al., 2004). However, the location of mei-yu front determinates the direction of error propagation.

6. Vertical structure of errors and the moist atmosphere

In this section the vertical structure of errors and its relationship with the moist atmosphere are discussed. Similar to the analysis in section 4, the difference total energy is defined as in Eq. (1), but using only a calculation of the mean of the horizontal DTE at different heights (hereafter HDTE), and covering about an area of $220{\times}220\ km^2$, including the whole convective system. The horizontal calculation region is defined by the center of the convective system at the different stages of convection. Figure 12 shows the vertical profiles of HDTE at the different convective stages, where the calculation region of the rain water and the cloud water is the same as for HDTE, but the calculation region of the divergence only covers about $110{\times}110\ km^2$ area, including the convective system center, because the horizontal scale of divergence is smaller than that of the HDTE. In fact, corresponding to the multi-step error growth discussed in section 5, MCS development in this event can be divided into three stages: the developing, mature, and renewing convective system. To investigate the overall characteristics of the errors in the vertical direction for the three stages of MCS development, the vertical profile of error in non-convection areas is also given. The time for the vertical profile calculation at the different stages is based on the development of convective systems. As shown in Fig. 12, the HDTE has a different vertical profile at each different stage, due to the differences in convective intensity at each height.

There is one peak of HDTE in the vertical near the non-convection area (Fig. 12a). This peak lies near the height of 700 hPa where the cloud water has one maximum, but the horizontal divergence and rain water are relatively small. This means that the HDTE growth in this area mainly depends on moist heating at this time, though the convection in this area is weak. During the developing stage of the convective system, there are two peaks of HDTE near the convective area (Fig. 12b). One is located between 850–700 hPa where the maximum divergence overlaps with it; the other is near the height of 300 hPa where the rain water reaches the maximum. In general, the maximum of the horizontal convergence indicates the convective intensity is strongest, and the rain water maximum implies moist convection is active. When the convective system becomes mature, there are also two peaks for HDTE (Fig. 12c). The lower peak of HDTE moves near the height of 925 hPa where the horizontal divergence is positive. The positive divergence is introduced by the sinking of the cold air, which is attributed to the evaporation of falling rain. The differences of the gust front of the cold pool contribute to this lower peak of HDTE (Fig. 12c). With the convective system decreasing, the lower peak decays in amplitude, but grows steadily in the horizontal scale as discussed in section 5. In the meantime, the old convective system may generally trigger a new one along its boundary. Figure 12d shows the vertical profile of HDTE at the time for the old convective system weakening and new one initially developing. There are also two peaks for HDTE, but the upper-level peak locates near the height of 200 hPa (Fig. 12d). Compared with Figs. 12b and 12c, the HDTE is relatively small in this period, due to weak convective instability. Though the old convective system is decreasing in strength, the upper-level vertical motion still stays large and the errors can be transported up higher, so that the upper-level peak of HDTE lies near the height of 200 hPa, which is higher than that in the developing stage (Fig. 12d).

Figure 13 shows the HDTE in different layers, i.e., low-, middle-, and upper-layers respectively: the boundary layer (1000–850 hPa), middle moist-convective layer (800–400 hPa), and upper moist-convective layer (400–100 hPa). The HDTE in the boundary layer has not reached the decaying stage, because there is enough water vapor in the boundary layer of the mei-yu front, and the moist convection starts up earlier in the low layer. During the transitional stage between a new and old MCS, the HDTE in the low- and middle- layers grows more slowly than that in upper-layer. The friction in the boundary layer is so strong that the HDTE in this layer could not continue growing after the convective motion decayed. The upward transport of errors and of the cloud water maintains the growth of the upper-layer HDTE.

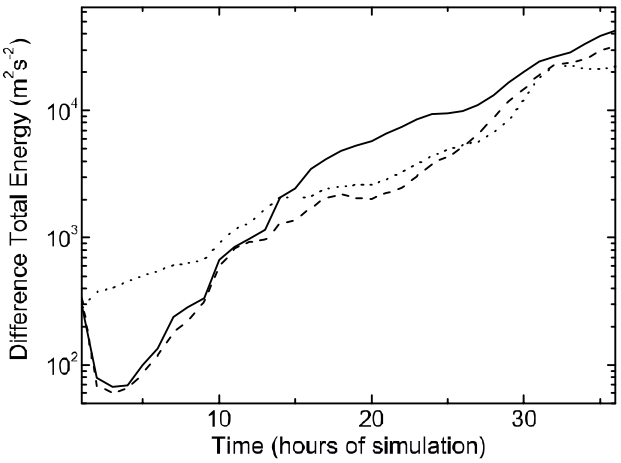

Fig. 13. The DTE (m^2 s^{-2}) evolution with the time in low-layer (1000–800 hPa; dotted line), middle-layer (800–400 hPa; dashed line) and upper-layer (400–100 hPa; solid line).

7. Summary and discussion

The present work explores the mesoscale predictability and error growth of precipitation episodes associated with the mei-yu front. Analyzing the evolution of errors as the difference between a control simulation and a simulation with perturbed initial conditions using the MM5, it is found that the mechanism of error growth canbe attributed to strong moist convective instability and weak baroclinicity related to the mei-yu front.

Synoptic-scale forcing from the mei-yu front indirectly plays a role on the heavy rainfall by moistening the environment and creating a favorable wind shear region. The cold pool and mesoscale convective vortex, resulting from the internal mesoscale forcing, may be responsible for the formation of coherent precipitation patterns. These characteristics could reduce the error growth rate compared with that in moist baroclinic systems. These features are similar to the observational analysis for warm-season coherent rainfall in North America reported by Carbone et al. (2002). The scale interaction within the mei-yu font makes the peak of the DTE spectrum obscure compared with that in ZSR03 and Tan04.

The error growth in mei-yu heavy rainfall concentrates inside mei-yu front, and closely relates to moist convective instability. The error distribution corresponds to the convective region, which again supports

the hypothesis that moist convection is responsible for the rapid error growth in mesoscale precipitation systems. The active low- and mid-level convective motion results in the vertical peak of error at 800–700 hPa for the developing convective system.

The quasi-stationary subsynoptic characteristic of the mei-yu front limits the distribution and growth of error, and the different evolution of MCSs along the mei-yu front results in different stages of error growth. The error growth in mei-yu heavy rainfall includes two components, one related to the growth of the amplitude, and another related to the growth of the horizontal scale. The scale interaction results in a multi-step error growth pattern in the mei-yu frontal heavy rainfall event.

According to the patterns of error growth in the amplitude and the scale, the growth of errors could be decomposed into three stages. In the first stage, the amplitude and scale of errors synchronously grow, but the error growth mainly appears as a result of the increase in amplitude, and mainly due to convective instability. In this stage, the convective system is in the developing phase and the error growth localizes in the low- and mid-level. The following stage reflects the upscale growth of errors, and the horizontal scale of error grows exponentially due to the convective heating. In the meantime, the growth in errors stemming from the amplitude decreases due to convective decay. In the third stage, the growth of the horizontal scale of errors is limited by the mei-yu front, and reaches saturation. Therefore, the horizontal scale of error is maintained at about 240 km, corresponding to the cross-frontal scale. In this stage, additional error growth appears with the increase of amplitude due to new MCS development. The growth rate of the amplitude accompanies the convective action, which further reinforces the above result that moist convection is responsible for the rapid growth of errors in mesoscale precipitation systems.

In a future study we intend to construct an idealized experiment about mei-yu heavy rainfall so that we can generalize these results from this single case study. The mechanisms of error growth found from these experiments will supply the background errors of an assimilation experiment, and will inform the member design of an ensemble prediction.

Acknowledgements. This research was supported by the National Key Scientific and Technological Project 2006BAC02B03, 2004CB418300, under the FANEDD 200325, The Specialized Research Fund for the Doctoral Program of Higher Education (20080284019), and National Natural Science Foundation of China under Grant No. 40325014.

REFERENCES

Akiyama, T., 1990: Large, synoptic and mesoscale variations of the Baiu front, during July 1982 Part II: Front structure and disturbances. *J. Meteor. Soc. Japan*, **68**, 557–574.

Anthes, R. A., Y. H. Kuo, D. P. Baumhefner, R. P. Errico, and T. W. Bettge, 1985: Predictability of mesoscale atmospheric motions. *Adv. Geophys.*, **28B**, 159–202.

Bei, N., and F. Zhang, 2007: Impacts of initial error scale and amplitude on the mesoscale predictability of heavy precipitation along the mei-yu front of China. *Quart. J. Roy. Meteor. Soc.*, **133**, 83–99.

Betts, A. K., and M. J. Miller, 1986: A new convective adjustment scheme, Part 2: Single column tests using GATE wave, BOMEX, ATEX arctic air-mass data sets. *Quart. J. Roy. Meteor. Soc.*, **112**, 693–709.

Blackadar, A. K., 1979: High resolution models of the planetary boundary layer. *Advances in Environmental Science and Engineering*, **1**, 50–85.

Carbone, R. E., J. D. Ruttle, D. A. Ahijevych, and S. B. Trier, 2002: Inferences of predictability associated with warm season precipitation episodes. *J. Atmos. Sci.*, **59**, 2033–2056.

Chu, K. K., Z.-M. Tan, and M. Xue, 2007: Impact of 4DVAR assimilation of rainfall data on the simulation of mesoscale precipitation systems in a mei-yu heavy rainfall event. *Adv. Atmos. Sci.*, **24**, 281–300. doi: 10.1007/s00376-007-0218-9.

Dudhia, J., 1993: A nonhydrostatic version of the Penn State-NCAR mesoscale model: Validation tests and simulation of an Atlantic cyclone and cold front. *Mon. Wea. Rev.*, **121**, 1493–1513.

Errico, R., and D. Baumhefner, 1987: Predictability experiments using a high-resolusion limited-area model. *Mon. Wea. Rev.*, **115**, 488–504.

Fritsch, J. M., and Coauthors, 1998: Quantitative precipitation forecasting: Report of the Eighth Prospectus Development Team, U.S. Weather Research Program. *Bull. Amer. Meteor. Soc.*, **79**, 285–299.

Liao, J., and Z.-M. Tan, 2005: Numerical simulation of a heavy rainfall event along the mei-yu front: Influences of different scale weather systems. *Acta Meteorologica Sinica*, **63**, 771–788. (in Chinese)

Lorenz, E. N., 1969: The predictability of a flow which possesses many scales of motion. *Tellus*, **21**, 289–307.

Molteni, F., and T. N. Palmer, 1993: Predictability and finite time instability of the northern winter circulation. *Quart. J. Roy. Meteor. Soc.*, **119**, 269–298.

Olson, D. A., N. W. Junker, and B. Korty, 1995: Evaluation of 33 years of quantitative precipitation forecasting at the NMC. *Wea. Forecasting*, **10**, 498–511.

Snyder, C., R. M. Hamill, and S. Trier, 2003: Linear evolution of forecast error covariance in a quasi-geostrophic model. *Mon. Wea. Rev.*, **131**, 189–205.

Tao, S. Y., 1980: *Heavy Rainfalls in China*. Science Press, Beijing, 225pp. (in Chinese)

Tan, Z.-M., F. Zhang, R. Rotunno, and C. Snyder, 2004: Mesoscale predictability of moist baroclinic waves:

Experiments with parameterized convection. *J. Atmos. Sci.*, **61**, 1794–1804.

Thompson, P. D., 1957: Uncertainty of initial state as a factor in the predictability of large scale atmospheric flow patterns. *Tellus*, **9**, 275–295.

Tribbia, J. J., and D. P. Baumhefner, 2004: Scale interactions and atmospheric predictability: An updated perspective. *Mon. Wea. Rev.*, **132**, 703–713.

Tuttle, J. D., and R. E. Carbone, 2004: Coherent regeneration and the role of water vapor and shear in a long-lived convective episode. *Mon. Wea. Rev.*, **132**, 192–208.

Wang, C.-C., G. T-J. Chen, and R. E. Carbone, 2004: A climatology of warm-season cloud patterns over east Asia based on GMS infrared brightness temperature observations. *Mon. Wea. Rev.*, **132**, 1606–1629.

Zhang, F., C. Snyder, and R. Rotunno, 2002: Mesoscale predictability of the "surprise" snowstorm of 24–25 January 2000. *Mon. Wea. Rev.*, **130**, 1617–1632.

Zhang, F., C. Snyder, and R. Rotunno, 2003: Effects of moist convection on mesoscale predictability. *J. Atmos. Sci.*, **60**, 1173–1185.

Zhang, F., A. M. Odins, and J. W. Nielsen-Gammon, 2006: Mesoscale predictability of an extreme warm-season precipitation event. *Wea. Forecasting*, **21**, 149–166.